Breaking Abbe's diffraction resolution limit in fluorescence microscopy with stimulated emission depletion beams of various shapes

Thomas A. Klar, Egbert Engel, and Stefan W. Hell*
High Resolution Optical Microscopy Group, Max-Planck-Institute for Biophysical Chemistry, 37070 Göttingen, Germany
(Received 7 May 2001; published 26 November 2001)

We report on the generation of various hole-centered beams in the focal region of a lens and investigate their effectiveness to break the diffraction barrier in fluorescence microscopy by stimulated emission. Patterning of the phase of the stimulating beam across the entrance pupil of the objective lens produces point-spread-functions with twofold, fourfold, and circular symmetry, which narrow down the focal spot to 65–100 nm. Comparison with high-resolution confocal images exhibits a resolution much beyond the diffraction barrier. Particles that are only 65-nm apart are resolved with focused light.

DOI: 10.1103/PhysRevE.64.066613 PACS number(s): 42.30.−d, 42.25.−p, 42.79.−e

I. INTRODUCTION

The limited spatial resolution in *far*-field light microscopy is a prominent physical problem with important consequences in the other natural sciences, particularly in biology, where far-field light microscopy remained the only method to visualize the cellular interior in three dimensions. The light microscope's limited spatial resolution was first recognized by Ernst Abbe at the end of the 19th century and has been paradigmatic ever since [1]. Abbe found that objects closer than about one-third of the wavelength of light could not be distinguished, because this is the smallest focal spot size that is allowed by diffraction when focusing with a lens of high numerical aperture [2]. As any great challenge, beating the diffraction limit preoccupied a number of preeminent scientists in physical optics. In 1952 Toraldo di Francia put forth an interesting concept, which in principle could provide noteworthy subdiffraction resolution [3]. However, a practical resolution increase with this concept is precluded by tradeoffs and requirements that are hard to meet. The far-field microscopy diffraction limit largely remained an unsurmountable reality.

A concept with which it has become possible to break the diffraction resolution limit in far-field *fluorescence* microscopy is stimulated emission depletion (STED) microscopy [4–6]. The basic idea of STED fluorescence microscopy is to inhibit the *spontaneous* emission at the periphery of the diffraction-limited spot of a scanning confocal microscope by *stimulated* emission [4]. The net result is a fluorescence spot, i.e., an effective point-spread-function (PSF) of the microscope, that is smaller than the dimensions set by diffraction. Recently, an axial resolution increase by up to a factor of 2–6 over the diffraction limit has been demonstrated by STED [6–8]. In these experiments the stimulating beam either formed a doughnut mode in the focal plane with intense lobes above and below [7], or the stimulating beam was simply offset in the lateral direction [6,8]. Whereas with this doughnut mode it was possible to attain a lateral resolution increase by a factor of ~2 in the radial direction and 6 in the axial direction, the simpler arrangement of an offset beam produced a factor of 2 along the axis of the offset and 2.5 in the axial direction. Under ideal conditions STED could provide far-field fluorescence microscopy resolution on the molecular scale. Therefore, the experimental investigation of the power and limitations of this concept is a fascinating field for fundamental and practical reasons. In this paper, after a brief introduction to the foundations of the STED concept, we report on the realization of doughnut-mode laser fields for STED and on the marked breaking of the diffraction barrier that is associated with these fields. Improved spatial resolution is of great value in the biological sciences, because by covering about 80% of all microscopy applications, fluorescence is the most widely applied imaging mode in biological research.

II. THEORY

In STED fluorescence microscopy two issues have to be solved. The first is spectroscopic and aims at realizing a set of conditions that enables the complete depletion of the excited state by stimulated emission; the second is optical and encompasses the spatial shaping of the stimulating beam, so as to render a focal spot with a central hole.

A. Spectroscopy

Meeting the spectroscopic conditions is based on the fact that virtually all fluorescent markers are four-level systems. Taking this into consideration, excitation and stimulated emission are carried out through consecutive laser pulses: a subpicosecond pulse exciting the dye is followed by a red-shifted picosecond pulse for stimulated emission depletion [4,9]. The latter is here referred to as the STED pulse. Whereas the wavelength of the subpicosecond excitation pulse is centered in the absorption spectrum of the dye, that of the STED pulse is placed in the red edge of the emission spectrum. The role of the STED pulse is to couple the dye's fluorescent state to a higher vibrational level of the ground state. The rapid vibrational decay (<500 fs) of the latter ensures that the inversion between the fluorescent and the ground state is maintained, so that the red-shifted pulse empties the fluorescent level effectively [4]. The depletion rate of

*Email address: hell@4pi.de

the fluorescent level increases with the intensity of the STED pulse. If we denote the population of the fluorescent state with N_1, that of the vibrational level of the ground state with N_0^*, and the local intensity with $h^{\mathrm{STED}}(t)$, the temporal evolution of these states is found by analyzing the following set of differential equations:

$$dN_1/dt = -N_1\sigma h^{\mathrm{STED}}(t)/\hbar\omega + N_0^*\sigma h^{\mathrm{STED}}(t)/\hbar\omega - N_1 k_{fl}, \tag{1}$$

$$dN_0^*/dt = N_1\sigma h^{\mathrm{STED}}(t)/\hbar\omega - N_0^*\sigma h^{\mathrm{STED}}(t)/\hbar\omega - N_0^* k_{\mathrm{vib}}, \tag{2}$$

where $\hbar\omega$ is the photon energy and k_{fl} and k_{vib} are the spontaneous emission (fluorescence) and vibrational relaxation rates, respectively. σ is the molecular cross section for the transition induced by the STED pulse. The first and second term on the right-hand side of Eq. (1) describe the stimulated emission from the fluorescent state and the re-excitation by the stimulating beam, respectively. The last term of Eq. (1) describes the decay of N_1 by spontaneous emission. Its counterpart in Eq. (2) describes the vibrational decay of N_0^*. If the focal intensity is low enough as to render the rates of the stimulated transitions much slower than k_{vib}, re-excitation is negligible and $N_0^* \approx 0$. Hence, for a given duration τ of an assumed rectangular STED pulse

$$h^{\mathrm{STED}}(t) = \begin{cases} h_0^{\mathrm{STED}} & \text{for} \quad 0 \leqslant t \leqslant \tau \\ 0 & \text{else} \end{cases} \tag{3}$$

the population of the fluorescent state and the remaining fluorescence obeys the proportionality $N_1(\tau) \propto \exp(-\sigma\tau h^{\mathrm{STED}}/\hbar\omega)$. For higher intensities the depletion of N_1 is determined by the fast vibrational relaxation alone ($k_{\mathrm{vib}} \geqslant 2\times 10^{12}\,\mathrm{s}^{-1}$). Altogether, this leads to a highly nonlinear relationship between $N_1(\tau)$ and h^{STED} which can be calculated numerically [5] or measured directly [7]. This nonlinear dependence is essential for overcoming the diffraction barrier.

B. Optics and beam shaping

In the focal region the local intensities of the excitation and the STED pulse vary according to diffraction. A thorough calculation of the intensities requires the consideration of the vectorial properties of light. Applying the Debye integral for linearly polarized illumination with a polarization angle ϕ_0 with respect to the x axis, the intensity distribution in the focal region (I-PSF) of an aplanatic lens can be calculated as follows [10,11]:

$$h^{\kappa}(\vec{r},t) = \frac{cn\varepsilon_0}{2}|\vec{E}^{\kappa}(\vec{r},t)|^2 = \frac{cn\varepsilon_0}{2}\left|\begin{pmatrix} E_x^{\kappa} \\ E_y^{\kappa} \\ E_z^{\kappa} \end{pmatrix}\right|^2 = \frac{n^3 c\varepsilon_0}{2\lambda^2}\left|\int_0^{\alpha}\int_0^{2\pi} E_0^{\kappa}(\theta,t)\sqrt{\cos\theta}\sin(\theta)\exp\{i[\Psi^{\kappa}(\theta,\phi)+ks-kf]\}\right.$$
$$\left.\times\begin{pmatrix} \cos^2(\phi-\phi_0)\cos(\theta)+\sin^2(\phi-\phi_0) \\ \sin(\phi-\phi_0)\cos(\phi-\phi_0)[\cos(\theta)-1] \\ -\cos(\phi-\phi_0)\sin(\theta) \end{pmatrix} d\phi\, d\theta\right|^2. \tag{4}$$

The superscript $\kappa = exc$ or STED stands for the excitation or STED beam, respectively. $\vec{E}^{\kappa}$ denotes the electric-field amplitude, c the speed of light, ε_0 the permittivity of free space, f the focal length of the lens, ϕ the azimuth angle, and θ the polar angle of the aperture, with $0 \leqslant \theta \leqslant \alpha$. The angle α is the half-aperture angle and $E_0^{\kappa}(\theta,t)$ is the wave front amplitude at the entrance pupil of the lens. The phase $\Psi^{\kappa}(\theta,\phi)$ denotes any arbitrarily induced phase change across the wave front; it equals zero if the wave front is spherical, as is here the case for excitation. s is the path traveled by the light from the point on the converging spherical wave front with the coordinates $[f,\theta,\phi]$, to the position $\vec{r}$ in the focal region. The focal point is located at $\vec{r}=[0,0,0]$. λ is the vacuum wavelength and $k = 2\pi n/\lambda$ the wave number, with n being the refractive index. For a given $\Psi^{\kappa}(\theta,\phi)$, Eq. (4) can be evaluated numerically.

The I-PSF defined by the illumination light is referred to as the excitation PSF. It is proportional to the local excitation rate and hence a measure of the size of the regular fluorescence spot. For excitation, we prefer a diffraction limited excitation PSF, that is we set $\Psi^{\kappa}(\theta,\phi)=0$. The redshifted STED beam, however, is ideally focused in such a way that the focal intensity distribution

$$h^{\mathrm{STED}}(\vec{r},t) = \begin{cases} 0 & \text{for} \quad \vec{r}=0 \\ \gg 0 & \text{else} \end{cases} \tag{5}$$

that is, the STED-PSF is zero in the center but strong at the periphery. This ensures that the center of the fluorescence spot defined by $h^{\mathrm{exc}}(\vec{r}=0)$ is spared out from depletion by stimulated emission, whereas its periphery is strongly depleted. Therefore, we prefer to investigate the time-averaged depletion efficiency $\varepsilon(\vec{r})$ rather than just the intensity $h^{\mathrm{STED}}(\vec{r})$. It is defined by [12]

$$\varepsilon(\vec{r}) = \varepsilon[h^{\mathrm{STED}}(\vec{r})] = 1 - \frac{\int dt\, N_1[t,\vec{r},h^{\mathrm{STED}}(t,\vec{r})]}{\int dt\, N_1(t,\vec{r},0)} \tag{6}$$

with $N_1(t,\vec{r},h^{\mathrm{STED}})$ being the population of the fluorescent level when subjected to a STED pulse. $N_1(t,\vec{r},0)$ is the population of the same state with vanishing STED beam intensity. $\varepsilon=1$ means that the fluorescent level is emptied completely.

Clearly, the focal intensity distribution of the zero-centered STED beam will also be limited by diffraction, so that the requirements set by Eq. (5) can only be fulfilled within the diffraction limits. Therefore, we decide to investigate and apply various beam shapes with a vanishing focal point intensity at the submicron scale. A zero-centered STED-PSF is realized, for example, through $\Psi^{\mathrm{STED}}(\theta,\phi)=\mathrm{sign}[\sin(\theta-\theta_0)]\pi/2$ with $\theta_0=\arcsin(\sin\alpha/\sqrt{2})$ dividing the wave front into two shifted circular areas of equal total amplitude. As a result a STED-PSF $h_0^{\mathrm{STED}}(\vec{r})$ is formed featuring two maxima on the optic axis above and below the focal plane, as well as a cylindrically shaped side maximum surrounding the optic axis. Employing $h_0^{\mathrm{STED}}(\vec{r})$, we have reduced the diffraction limited focal spot from its initial values of 250 and 600 nm full width at half maximum (FWHM) in the lateral and axial direction, respectively, to about 100 nm in all directions [7]. Here we report on the creation of forms of hole-centered STED-PSF and explore their efficiency to break the diffraction resolution barrier. Moreover, we apply the subdiffraction focal spots to the separation of identical particles to establish a new resolution benchmark in far-field microscopy.

III. SETUP

Ultrafast pulses of 140 fs duration are provided by a mode-locked titanium:sapphire laser (Mira 900, Coherent, Santa Clara, Ca) running at a wavelength of 765 nm. A part of the beam is converted into a 558 nm beam by an optical parametric oscillator with intracavity second-harmonic generation (APE, Berlin, Germany) which is used for excitation. The not converted part of the laser beam is used for STED. For this purpose, the 140 fs pulses are stretched by a grating to several tens of ps to render STED efficient [4,6]. A delay stage ensures that the STED pulses arrive at the sample right after the excitation pulses. Both pulse trains are initially polarized in the x direction and coupled into an optical setup (Fig. 1) which is basically a piezo-stage scanning confocal fluorescence microscope, adapted for the needs of STED. A 100× magnifying oil immersion lens (Leica Planapo) of 1.4 numerical aperture is used, providing the highest aperture angle of all aberration-corrected lenses available. The pinholes (PH) and the lenses deliver flat illumination wavefronts for both beams. The pinhole diameter and the focal length of the lenses are indicated in Fig. 1.

In the first set of experiments, we utilized a single STED beam, indicated in Fig. 1 as a solid line, featuring x-oriented polarization ($\phi_0=0°$). For this purpose, the λ/2 retardation plate drawn in Fig. 1 was removed; the polarizing beam splitters PBS1 and PBS2 were transparent for the x polarization. The wave-front modification was accomplished by a single binary phase plate PP1 producing an upper- and a lower-half wave front delayed by π against each other, that is the dividing line was set parallel to the polarization. In the second set of experiments, we inserted the λ/2 retardation

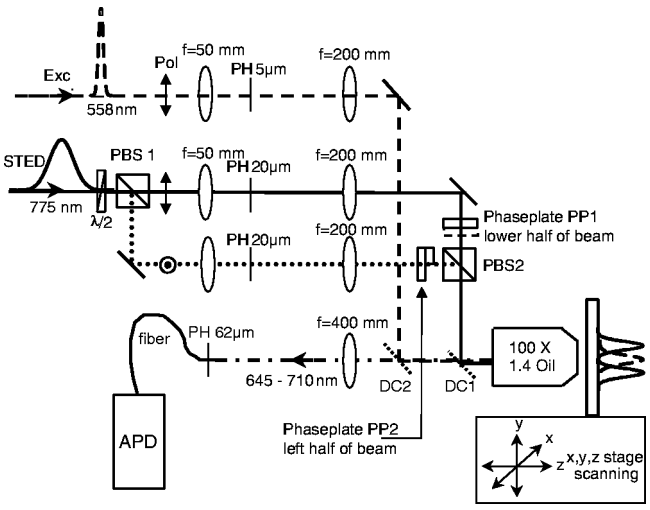

FIG. 1. STED microscope. The x-polarized excitation (Exc.) and depleting (STED) beams are cleaned and expanded by PH and suitable lenses of focal length f. The beams are coupled into the objective lens by means of dichroic mirrors (DC1 and DC2). When using a single STED beam, only the upper STED beam (solid line) is applied; its wavefront is modified by the phase plate PP1. By dividing the initial beam into two parts, a second STED beam can be added (dotted line). This is accomplished by rotating the polarization of the incoming STED beam with a λ/2 retarder and subsequent division (PBS1) and recombination (PBS2) of the two beams with polarizing beam splitters, as in a Mach-Zehnder interferometer. The fluorescence light generated in the sample passes through the dichroic mirrors and is directed onto the opening of a fiber serving as a confocal pinhole. It is detected by a counting avalanche photodiode. Images are recorded by scanning the sample with a piezo stage. Confocal reference images were taken by intercepting the STED beam.

plate and modified the STED beam in a Mach-Zehnder interferometer [13,14]. PBS1 formed two wave fronts of equal amplitude but orthogonal polarization. Whereas the x-polarized ($\phi_0=0°$) part was transmitted, the y-polarized wave front ($\phi_0=90°$) was directed along the path sketched as a dotted line. PP2 is identical with PP1, but rotated by 90°, so that the lines of division between the delayed and undelayed halves of the extended beams are parallel to the polarization in each arm. The phase delay was technically accomplished by a MgF_2 ($n=1.382$) layer evaporated onto a substrate of crown glass (BK7). Layers of 1 μm thickness induced a phase delay of π at the STED wavelength of 765 nm.

The fluorescence light was collected by the objective lens. After having passed the dichroic beam splitters DC1 and DC2, it was filtered out and focused onto the opening of a glass fiber, which in turn fed the light into a counting avalanche photodiode. The optical magnification of the detection path was chosen such that the 62 μm diameter fiber opening acted as a confocal pinhole with a diameter of twice the back-projected main diffraction maximum of $h^{\mathrm{exc}}(\vec{r})$. When the STED beam was blocked the setup acted as an ordinary confocal fluorescence microscope. Neglecting the finite size of the pinhole, the effective point-spread-function (E-PSF) of the microscope is then given by

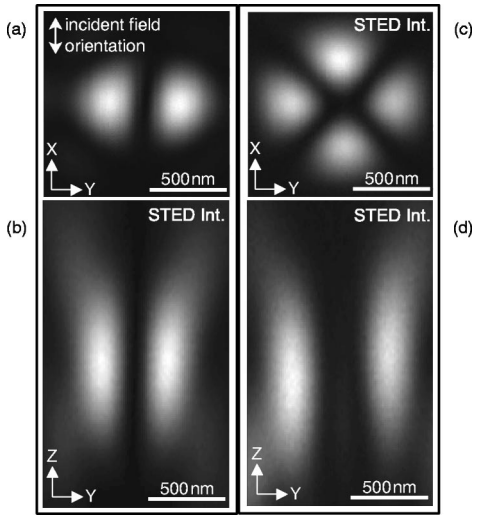

FIG. 2. STED-beam PSF for single STED beams produced by a binary phase plate PP1, recorded at a wavelength of 765 nm and a 1.4 nominal numerical aperture. PP1 reverts the sign of the amplitude in one-half of the entrance pupil. Panels (a) and (b) show the *xy* and *yz* sections, respectively. The plane defined by $y=0$ is a nodal plane. In panels (c) and (d) another PP1 is applied that alternates the sign in neighboring quadrants. Panels (c) and (d) depict the *xy* and *yz* sections of the resulting STED-beam PSF, respectively. Here, the $\pm 45°$ planes are planes of vanishing intensity. Note that in (c) and (d) the central hole is larger than in (a) and (b).

$$h^{\mathrm{conf}}(\vec{r}) = h^{\mathrm{exc}}(\vec{r}) h^{\mathrm{det}}(\vec{r}), \tag{7}$$

$$h^{\mathrm{exc}}(\vec{r}) = \frac{1}{T}\int_0^T h^{\mathrm{exc}}(t,\vec{r})\,dt, \tag{8}$$

$$h^{\mathrm{det}}(\vec{r}) = \frac{cn\varepsilon_0}{4\pi}\int_0^{2\pi} |E(\vec{r})|^2\,d\phi, \tag{9}$$

with T much greater than the duration of the excitation pulse and h^{det} calculated at the fluorescence emission wavelength. We note that the prefactors in Eqs. (8) and (9) are given for completeness; they are irrelevant for the calculation of the E-PSF, which is essentially a spatial weighting function quantifying the normalized probabilities for a point $\vec{r}$ to contribute to the detected signal. The narrowing through STED of the diffraction limited fluorescence spot resulting from $h^{\mathrm{exc}}(\vec{r})$ reduces the focal extent to subdiffraction dimensions. The E-PSF of the STED microscope is given by

$$h^{\mathrm{eff}}(\vec{r}) = h^{\mathrm{exc}}(\vec{r}) h^{\mathrm{det}}(\vec{r})\{1-\varepsilon[h^{\mathrm{STED}}(\vec{r})]\}. \tag{10}$$

Thus, the time-averaged STED-efficiency distribution $\varepsilon[h^{\mathrm{STED}}(\vec{r})]$, given by Eq. (6), ''engineers'' the E-PSF of our microscope.

IV. RESULTS

A. Unidirectional valley of depletion

In the first experiment employing a single STED beam, the hole-centered STED-beam PSF $h_x^{\mathrm{STED}}(\vec{r})$ was produced by a binary phase plate PP1 and an *x*-polarized incoming beam, i.e., $\phi_0 = 0°$. The experimental result is an unidirectional valley of depletion oriented in the *x* axis, as shown in Figs. 2(a) and 2(b). The phase plate induced a phase lag of π between the upper- and lower-half of the incoming wave front corresponding to $\Psi^{\mathrm{STED}}(\theta,\phi) = \mathrm{sign}(\sin\phi)\pi/2$. The orientation of the $\vec{E}$ field along the separation line avoided a significant longitudinal field orientation in the valley, as can also be inferred from Eq. (4). We quantified $h_x^{\mathrm{STED}}(\vec{r})$ by probing it with a 100-nm gold bead adherent to a glass cover slip, covered with immersion oil. For this purpose nonconfocal detection was applied and the light scattered by the gold bead was recorded [7,15]. Figures 2(a) and 2(b) show $h_x^{\mathrm{STED}}(\vec{r})$ as sections through the *yx* and the *yz* plane, respectively. As a result of the wave front modification, $h_x^{\mathrm{STED}}(\vec{r})$ vanishes in the plane defined by $y=0$, which is interesting for decreasing the fluorescence spot size in the *y* direction. The increase in lateral resolution associated with $h_x^{\mathrm{STED}}(\vec{r})$ was quantified by recording *xy* images of subresolution sized agglomerations [6] (nanocrystals) of fluorescent molecules [Figs. 3(a) and 3(b)]. These nanocrystals were formed by drying a saturated solution of Pyridine 2 (Lambdachrome, Göttingen, Germany) on a standard glass coverslip as described in Ref. [6]. Figure 3(a) shows prominent circular spots taken with the STED beam switched off, representing the lateral resolution under high-resolution confocal conditions. The result is directly compared with that of Fig. 3(b) where the STED beam is switched on. In fact, the comparison is made line by line during the recording by switching the STED beam on and off in the backward and the forward line scan, respectively. The comparison reveals that for the applied average power $P_{\mathrm{ave}} = 27.6\,\mathrm{mW}$, which is associated with a peak power of 4.6 GW/cm^2 [7], the FWHM of the nanocrystal images is indeed reduced by a factor of 2.4 in the *y* direction, as shown in the fluorescence intensity line profiles of Fig. 3(c). The results testify to a marked decrease of the fluorescence spot beyond the diffraction limit in the *y* direction.

Since the decrease in spot size strongly depends on the STED beam intensity, we quantified the reduction in FWHM along the *y* axis as a function of the average STED beam intensity for a pyridine 2 nanocrystal. The results are depicted in Fig. 4 along with those for the ratio $\eta = h_{\mathrm{max}}^{\mathrm{eff}}/h_{\mathrm{max}}^{\mathrm{conf}} = 1-\varepsilon[h^{\mathrm{STED}}(\vec{r}=0)]$. The ratio η quantifies how the region around the geometric focal point is spared out from depletion by stimulated emission. In an ideal realization of STED microscopy, η equals unity, because $h^{\mathrm{STED}}(\vec{r}=0)=0$. Our measurements revealed values of η decreasing from unity (found at low intensities) down to 0.3, which is in reasonable agreement with our expectation. The reasons for the deviation from unity will be explained further down in the paper. As expected from theory [5], the FWHM decreases rapidly with increasing STED intensity. For high intensities, however, the decrease in intensity levels out around 65 nm, so that this appears to be the maximum resolution possible with this wavelength and dye.

So far, the narrowing of the E-PSF reported in this paper is achieved only in the *y* direction. Therefore, one might

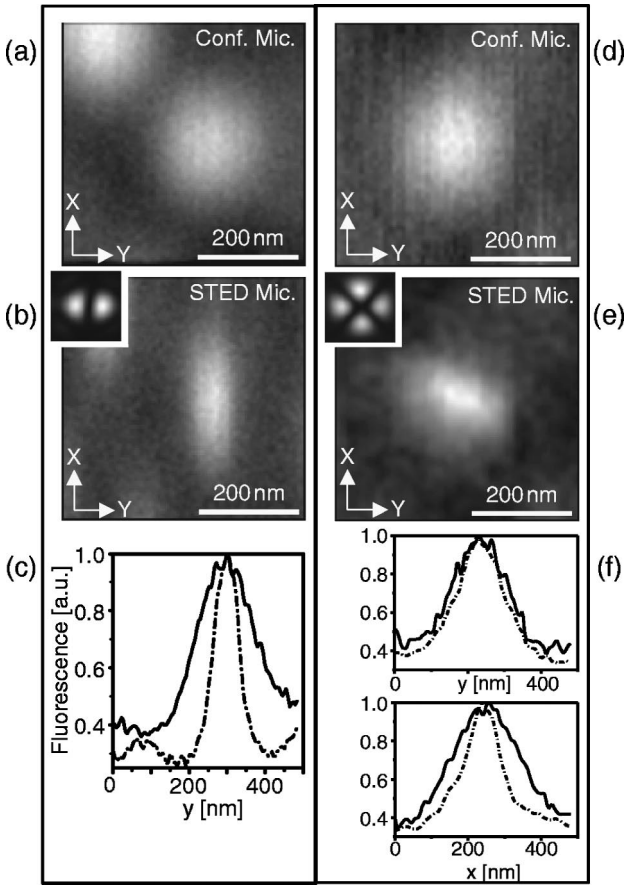

FIG. 3. Resolution improvement through single-beam STED [(b) and (e)] over confocal [(a) and (d)] microscopy demonstrated with nearly isolated subresolution fluorescent nanoparticles. Whereas for (b) the STED PSF of Figs. 2(a) and 2(b) was applied, the data in (e) were recorded using the quadrant-shaped STED-PSF of Figs. 2(c) and 2(d). Panel (c) depicts the fluorescence intensity in the *y* direction through the center of the central spot in (a) (solid line) and (b) (dash-dotted line); it reveals a 2.4 fold narrowing of the effective point-spread function along the *y* axis. (f) compares the fluorescence intensity profiles along the *x* and the *y* direction of the confocal (d) with those of the STED image (e). The comparison reveals that the STED-PSF of Figs. 2(c) and 2(d) is much less effective for resolution improvement than that of Figs. 2(a) and 2(b). The imaged particles were pyridine 2 nanocrystals (a)–(c) and 50 nm latex beads, dyed with LDS 751 (d)–(f).

think of applying a phase function with fourfold symmetry, $\Psi^{\mathrm{STED}}(\theta,\phi)=\mathrm{sign}[\sin 2(\phi-\pi/4)]\pi/2$, which produces valleys of depletion along the $\pm 45°$. Such a function is readily obtained by a phase plate with four quadrants, with neighboring quadrants featuring a phase shift of π (see Appendix A). The resulting STED-PSF $h_{x/y}^{\mathrm{STED}}(\vec{r})$ is shown in Figs. 2(c) and 2(d). The STED intensity is now distributed into four maxima along the *x* and *y* axis, but, as one can also show from a theoretical analysis, these maxima are now further apart from the focal point. Consequently, in the experimental application the quandrant-shaped STED beam proved to be less effective for increasing the spatial resolution; compare Figs. 3(d) with 3(e). The FWHM could only be decreased down to 115 and 140 nm in the *x* and *y* direction, respectively. This can also be inferred from Figs. 3(f) showing the fluorescence intensity profiles. The asymmetry in the *x* and *y* direction is due to a slight asymmetry of $h_{x/y}^{\mathrm{STED}}(\vec{r})$. In summary, the quadrant shaped $h_{x/y}^{\mathrm{STED}}(\vec{r})$ was identified as unsuitable and not further investigated.

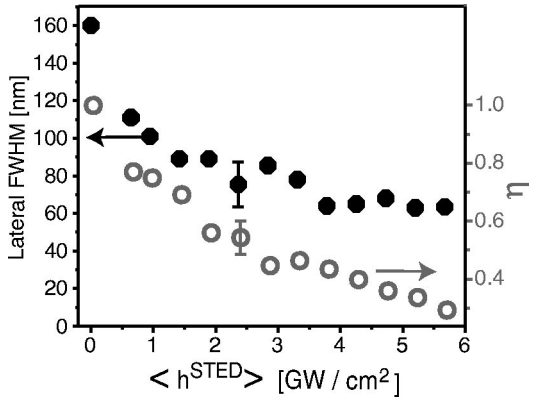

FIG. 4. Reduction of the extent of the effective PSF along the *y* axis as a function of the STED-beam intensity along with the concomitant signal at the geometric focal point η. Lateral full width half maxima down to 65 nm are obtained.

According to Eq. (10) the attainable spatial resolution is determined by $\varepsilon(h^{\mathrm{STED}})$ and, therefore, by the applied STED-beam intensity. In the measurements shown in Figs. 3 and 4 one cannot fully exclude that for high intensities the extent of the nanoparticles is non-negligible with respect to the extent of the effective fluorescence spot. Therefore, we investigated the spatial properties of $\varepsilon[h_x^{\mathrm{STED}}(\vec{r})]$ separately. Figure 5 shows again the measured $h_x^{\mathrm{STED}}(z=0)$ in (a) along with its profile $h_x^{\mathrm{STED}}(x,z=0)$ in (d). Figure 5(b) shows the measured $\varepsilon(h^{\mathrm{STED}})$ for pyridine 2. By combining these data we converted the STED intensity profiles into experimentally obtainable STED-efficiency profiles $\varepsilon[h_x^{\mathrm{STED}}(x,z=0)]$. Note that in the very center of h_x^{STED} the intensity is only 0.7% of the intensity found in the two maxima [Fig. 5(d)]. Hence, along the *y* axis $\varepsilon[h_x^{\mathrm{STED}}(\vec{r})]$ features a steep valley where fluorescence is not cancelled out by stimulated emission.

The profiles are depicted in Fig. 5(e) for various maximal intensities: 0.1, 0.5, 2.0, 4.6, and 10 GW/cm^2. Figure 5(c) depicts the most relevant part of the data on a magnified scale. As expected from theory [4] increasing the STED-beam intensity narrows down and steepens the edges of the STED-efficiency profile. Since the central spot of h_x^{STED} is not perfectly zero, an unlimited increase of the intensity leads to a suppression of fluorescence in the center, thus counteracting the reduction of the FWHM. We found that a peak intensity of 4.6 GW/cm^2 (bold line) was a good compromise. [This is also why we used this intensity in the experiment shown in Fig. 3(b)]. These data are important because the narrowest valley corresponds to the highest spatial resolution possible with this dye and STED-beam PSF. We found the narrowest valley to be 44 nm in FWHM. In terms of the used wavelength of 765 nm, this corresponds to a spatial resolution in the *y* direction of $\lambda/17$.

The common orientation of the $\vec{E}$ field and the dividing line between the two halves of the phase plate is critical,

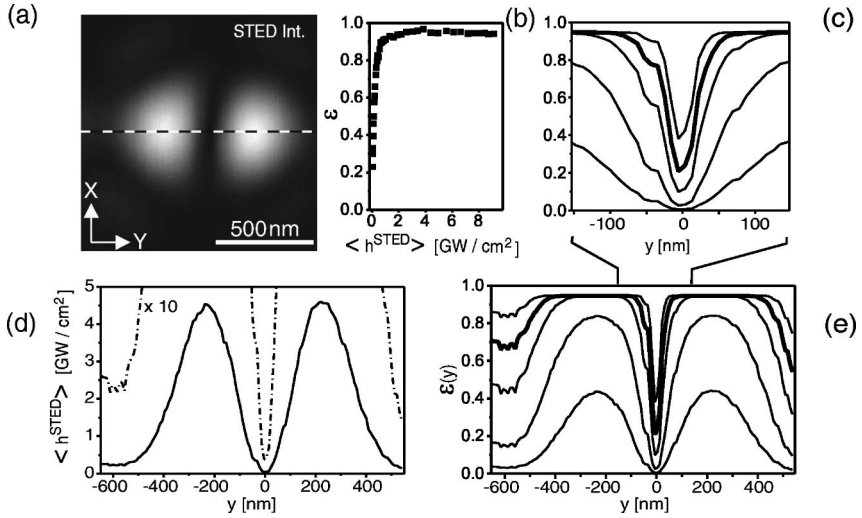

FIG. 5. Resolution potential of the (a) STED-beam PSF $h_x^{\mathrm{STED}}(x,y,0)$ of Fig. 2(a) explored by analyzing the spatial structure of the STED efficiency $\varepsilon[h_x^{\mathrm{STED}}(0,y,0)]$. Panel (d), intensity in the y direction; (b) STED efficiency $\varepsilon(h^{\mathrm{STED}})$; (e) profile $\varepsilon[h_x^{\mathrm{STED}}(0,y,0)]$ obtained by combining (d) and (b) and electing peak intensities of 0.1, 0.5, 2.0, 4.6 (bold), and 10 GW/cm^2. Increasing the STED intensity steepens the slopes of the STED efficiency, but at large intensities a residual depletion in the center becomes effective. Panel (c) is a magnification of the most relevant part of (e).

because the two phase-shifted halves of the wave fronts cancel each other out in this case only. If the polarization of the STED beam is rotated by 90°, the curvature of the focused wave front leads to the formation of a significant longitudinally polarized (z-) component effectively precluding the formation of a nodal plane. Indeed, upon rotation of the phase plate by 90°, the value around the focal point measured by the detector increased from 0.7% to about 7%.

Having investigated the effective point-spread functions, we investigated the separation capability of two adjacent objects. In the left-hand column of Fig. 6, we imaged two pyridine 2 nanocrystals that are slightly less than 100 nm apart, both in the confocal (a) as well as in the STED (b) microscopy mode. The pairs of images were obtained by switching the STED beam on and off, line by line. Panel (c) shows a line profile of the STED-confocal image in the y direction.

The right-hand panels (d) and (e) show two 30-nm polystyrene beads (Bangs Labs, Fishers, IN) stained with the dye LDS 751 (Molecular Probes, Eugene OR). Whereas the beads are undistinguishable in the confocal recording (d), its STED counterpart (e) and the line profile (f) reveal that they are only 65 nm apart. These objects are, to our knowledge, the closest spectrally identical particles ever resolved with a far-field microscope working in the visible range. We emphasize that the resolution improvement has been gained without the help of image processing. In terms of wavelength, this separation is of the order of λ/11.

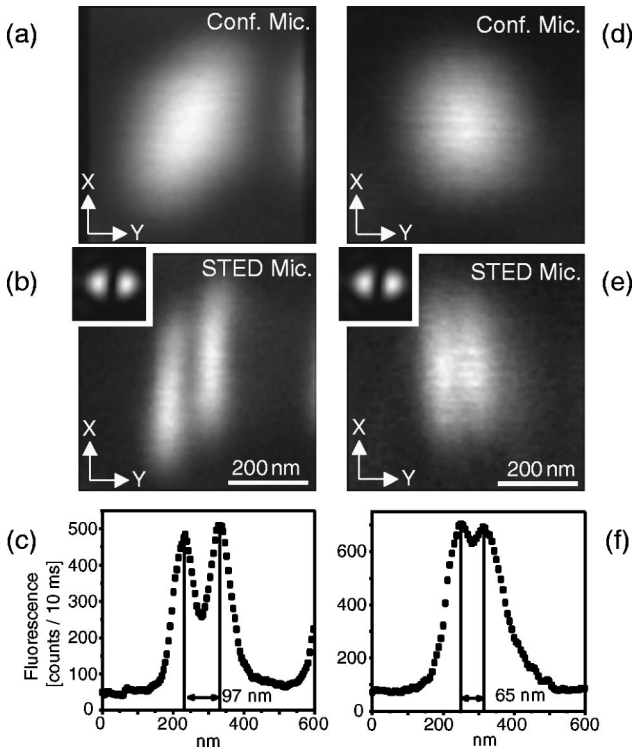

FIG. 6. Comparison of confocal images of nanoparticles [(a) and (d)] with their STED microscopy counterparts [(b) and (e)], whereby the STED-beam PSF of Figs. 2(a) and 2(b) is applied (inserts). While in (a) only an ellipticity is observed, in (b) the nanoparticles are resolved as entities with a 97 nm y distance. While the confocal image in (d) shows a circular spot, its STED counterpart distinguishes two particles at a distance of 65 nm in the y direction. Panels (c) and (f) display the intensity profiles in the y direction, extracted from the center of the STED images (b) and (e), respectively.

B. Radial two-dimensional valley of depletion

In order to squeeze the E-PSF from all transverse directions, we designed a doughnut-mode STED-beam PSF. For this purpose we divided the entering STED beam into two equal parts with orthogonal polarization, by means of a polarizing beam splitter (PBS1). The two arms of the interferometer were recombined by a second polarizing beam split-

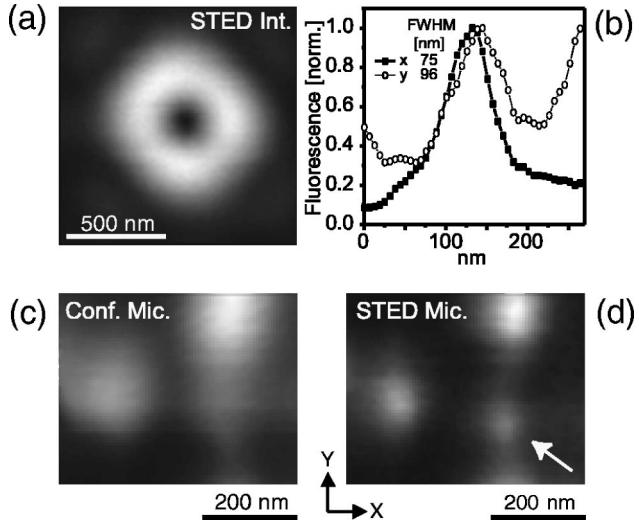

FIG. 7. (a) Shows a STED-beam PSF produced by two beams and binary phase plates in a Mach-Zehnder arrangement. Panel (c) is a confocal reference image for the thus produced STED-microscopy image of the pyridine 2 nanoparticles. Panel (b) shows the fluorescence intensity profiles of the nanoparticle indicated by the arrow in (d); the FWHM are 75 and 96 nm in the x and y direction, respectively. The somewhat broader FWHM in the y direction is largely due to contributions from a nearby particle.

ter (PBS2). In each arm we introduced a two-zone phaseplate with the dividing line oriented parallel to the specific field orientation [13,14]. While the first arm was x polarized ($\phi_0 = 0°$) with $\Psi^{\mathrm{STED}}(\theta,\phi) = \mathrm{sign}(\sin\phi)\pi/2$, the second was y polarized ($\phi_0 = 90°$) with $\Psi^{\mathrm{STED}}(\theta,\phi) = \mathrm{sign}(\cos\phi)\pi/2$. We carried out measurements both with the fields of the interferometer arms superimposed incoherently and coherently. In both cases, the total intensity is expected to be zero at the focal point. The resulting doughnut-mode STED-beam PSF was measured using a 100-nm gold bead. The result is shown in Fig. 7(a) for incoherent overlap of the two beams. The measurement confirms that it resembles a ring, such that one should expect the E-PSF to become narrower in all directions in the focal plane.

The concomitant resolution increase is demonstrated in Fig. 7 showing a confocal (c) and a STED image (d) of pyridine 2 nanoparticles on a cover slip. The image in Fig. 7(d) is substantially sharper than its confocal counterpart in Fig. 7(c). To quantify the FWHM, x and y profiles are given in Fig. 7(b). The profiles are extracted from the ''smallest'' nanoparticle in the image, indicated by an arrow. The FWHM is 75 and 96 nm in the x and y direction, respectively, which is narrower by a factor of 2–3 than what is expected from a diffraction limited system.

Finally, Figs. 8(a) and 8(b) reveal the improvement of resolution obtained by a doughnut-mode STED beam produced by coherent addition of the fields of the two arms of the Mach-Zehnder interferometer. Figure 8(b) shows a marked increase in resolution both in the x and y direction for all features imaged. A prominent object is the bright ''cluster'' in the center, which is not resolved in the confocal mode but recognized as consisting of at least four groups of molecular aggregations in the STED image. Figure 8(c) displays a sketch of the position of these aggregations and Fig. 8(d) exhibits the intensity profiles along the lines marked in Fig. 8(c). The pronounced dips in the intensity profiles underscore the subdiffraction resolution of the STED microscope.

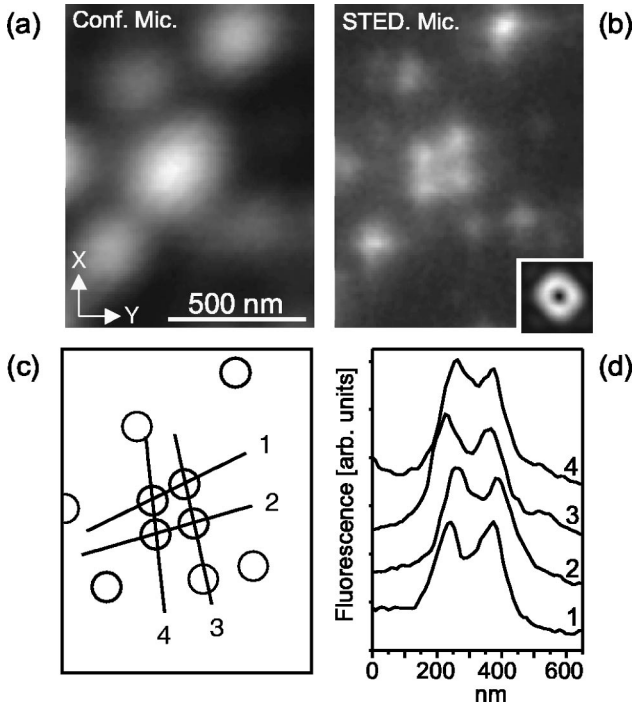

FIG. 8. Subdiffraction resolution in far-field fluorescence light microscopy by a doughnut-mode STED beam. The STED image in (b) is substantially better resolved than its high-end confocal counterpart in (a). The sketch in (c) depicts the position of dye aggregations as revealed by the STED image. Panel (d) displays the intensity profiles along the lines 1–4. The intensity profiles and the improved clarity in (b) underscore the subdiffraction resolution of the STED microscope.

V. DISCUSSION

Our experimental investigations have revealed for the first time the possibility of distinguishing spectrally identical objects at a distance of 65 nm in the far field. However, we note that according to our studies the resolution of our STED microscope is probably significantly better. Strong evidences along these lines are the STED-efficiency valleys $\varepsilon[h_x^{\mathrm{STED}}(\vec{r})]$ displayed in Fig. 5. Tracing back to the measured focal STED-beam intensity, the FWHM of the STED-efficiency valleys do not depend on the size of the test objects; they just quantify the spatial extent in which fluorescence is allowed. The finding that it is feasible to create FWHM that are as narrow as 44 nm indicates that the physical concept of STED microscopy should allow us to obtain a resolution of this order. This is still significantly better than what is indicated by the measurement in Fig. 4 showing an attainable lateral resolution of 65 nm.

A very plausible explanation of this apparent underperformance of the STED microscope is the simple fact that the extent of our test objects, that is the fluorescent nanocrystals,

was slightly too large. In other words, while the test objects were perfectly ''pointlike'' for the confocal microscope, they were probably not so for the STED microscope. This reasoning is further supported by the fact that in the same measurement, the ratio $\eta = h_{\max}^{\mathrm{eff}}/h_{\max}^{\mathrm{conf}}$ drops to 0.3 (Fig. 4). According to the STED efficiency $\varepsilon[h_x^{\mathrm{STED}}(\vec{r})]$ of Fig. 5 one would expect $\eta \sim 0.8$. (The bold line in Fig. 5 shows the STED efficiency at the used intensity.) If the measured nanocrystal is not pointlike but slightly more extended, one obtains an apparent larger reduction of the fluorescence. The reason is that a non-negligible fraction of the fluorescence of these finite-sized objects are suppressed by the slopes of the STED-efficiency valley. Our method of producing these nanocrystals did not allow us to *determine* the size of the ''nanocrystals,'' but only to establish an upper bound. The smallest nanocrystals were identified by selecting the faintest islands of fluorescence, that at the same time also exhibited the smallest extent in the confocal recording. Producing well-defined fluorescence structures at the sub-20-nm size scale is highly desirable but not straightforward. We are investigating these possibilities, along with the alternative possibility to image individual molecules.

The electric-field orientation has to be taken into account in two respects. First, the orientation of the incoming electric light field has to be adjusted with regard to the symmetry of the applied phase function. This orientation determines how well the electric field approaches zero at the geometric focal point. Second, according to the rules of photoselection for dipole transitions, the excitation beam creates a population of excited molecules with a particular orientational structure of the transition dipoles [16]. As most of the molecules are not freely rotating in the sample, the STED efficiency is largest if the polarization of the beam is the same as that of its excitation counterpart [17].

In the experiment with the Mach-Zehnder interferometer, the excitation with circularly polarized light is advisable. As far as the field orientation of the STED beam is concerned, it is interesting to discuss the effects of the various forms of superposition of the two wave fronts on the field orientation. Incoherent addition, as used for the experiments shown in Fig. 7, leaves an *x*- and *y*-polarized field for stimulated emission with two strong maxima along the *y* and *x* direction, respectively. In the case of coherent superposition, the orientation of the resulting field is a function of the relative phase of the two beams. For a phase difference of a multiple of 2π, the field orientation is nearly tangential. It would be tangential if the amplitudes of the two arms were proportional to $\sqrt{\cos\phi}$ and $\sqrt{\sin\phi}$, respectively [13]. This is not the case since we illuminated with a planar wave front, which leaves a $\sim$5% tangential modulation of intensity in the focus. Apart from focusing imperfections, the lack of this azimuthal dependence might also be one of the reasons why our doughnut modes show a small nonuniformity at a given radial distance. The orientational distribution also slightly changes with phase. However, since we drive the stimulated emission into saturation, the effect of the intensity nonuniformities are of minor importance. The introduction of an azimuth dependent amplitude would have required elaborate amplitude filters, but hardly changed the overall situation. The Mach-Zehnder setup is attractive because it always features zero intensity in the center, irrespective of incoherent or coherent addition, or relative phase of the wave fronts. Fine details of the STED-PSF will also depend on residual aberrations introduced by the objective lens or by the sample. The aberrations introduced on the excitation PSF, however, are of minor importance since the outer parts of the fluorescence spot will be quenched. In fact, their fine structure is so insignificant, that one can optimize the microscope towards achieving the most effective beam shape for the STED beam.

In contrast to the circular step function created mode [7], the present doughnut mode is optimized for maximizing the transverse resolution. Whereas in the latter, the first-order ring-shaped maximum is accompanied by a series of higher-order ring-shaped side maxima spreading the intensity in the focal plane, the presnet doughnut mode advantageously concentrates 4–5 times more stimulating photons in the first ring. Thus a higher stimulating beam intensity is achieved for confining the fluorescent spot. This advantage is bought at the expense of a lack of axial confinement, but it is clear that in order to simultaneously achieve a marked increase in resolution in the axial direction as well, one could apply two or more STED pulses consecutively. For example, the pulse intensity distribution of Fig. 2 could be followed by another one with strong axial intensity blobs or by pulses from laterally offset beams [4,6,8].

Other challenges for realizing STED microscopy are the potential level of photobleaching induced by the STED beam. In the measurements reported herein, the effect of photobleaching is small, which is evidenced by the fact that we recorded our image pairs and point-spread functions (Figs. 3 and Figs. 6–8) simultaneously, line by line. As the pixel size in the direction of the line offset is 5–10 times smaller than the extent of the focal STED-beam PSF, a significant photobleaching would have simply precluded the recording of the image pairs. Bleaching is also incompatible with the creation of sharper images. The reduction of the signal by stimulated emission has also been backed by ultrafast pump-probe experiments [6] as well as by the finding that the depletion efficiency changes with wavelength according to the emission spectrum of the dye. While the STED concept is, in principle, applicable to any organic molecule that can be described as a three- or four-level system, significant photobleaching can occur for other dyes and environments as a result of the high pulse energies of the STED beam. Detailed investigations are required to analyze to what extent the STED concept can be practically applied to other dye-environment conditions. These experiments are ideally carried out at the single molecule level.

VI. CONCLUSION

By modifying the phase across the entrance pupil of a lens, the focal intensity distribution of a beam inducing stimulated emission can be designed in such a way that it stops the fluorescence from the outer part of the focal spot, while leaving its center largely unaffected. Spatially selective depletion of the molecular excited state fundamentally

breaks the diffraction resolution barrier in far-field fluorescence microscopy.

Exploring various phase functions and arrangements we found that a unidirectional valley of depletion produces fluorescence spots that are narrowed down to 60–70 nm in full width at half maximum. The application of such a spot in a 1.4 numerical aperture objective lens allowed us to resolve two identical particles at a distance of only 65 nm. In terms of the used wavelength of 765 nm, this amounts to a transverse resolution of about an eleventh of the wavelength. A resolution of this order has hitherto only been reported with surface-bound near-field optical microscopy, but in contrast to the latter STED microscopy, being a far-field method, has a genuine three-dimensional imaging capability. Detailed investigations of the local distribution of the depletion efficiency revealed the possibility to achieve a far-field fluorescence microscopy resolution of the order of 45 nm.

The overlap of *two* beams in a Mach-Zehnder interferometer produced diffraction-limited, doughnut-shaped focal intensity distributions with a hole diameter of ~250 nm. Such a stimulating spot squeezed the extent of the microscope's effective point-spread function in both transverse directions (x,y) to a FWHM of about 85 nm, respectively. The increase in spatial resolution is demonstrated in images of fluorescent objects. Compared with high-end confocal fluorescence images, the images obtained through STED microscopy are vastly improved in clarity.

Our measurements indicate that the nonvanishing intensity in the center of the stimulating spot is the current limiting factor for achieving an even higher spatial resolution. Therefore, further significant improvements are expected from more elaborate wave front patterns, that lead to more pronounced local minimas in the center of the stimulating spot. Higher intensity contrasts would allow the application of even higher local intensity levels of the stimulating beam and hence may well lead to a far-field microscopy resolution in the range of 20–40 nm.

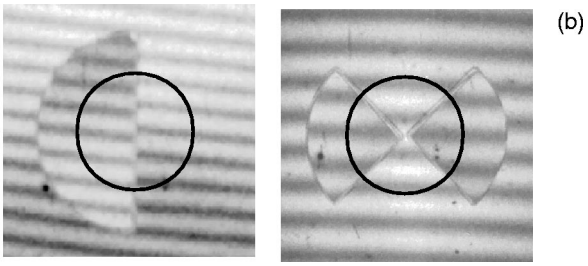

FIG. 9. Interferograms of phase retarding plates recorded at 644 nm. Binary phase plate with (a) half-dividing zones, (b) quadrant zones. The circle indicates the extent of the entrance pupil of the objective lens.

ACKNOWLEDGMENT

We thank W. Sauermann for manufacturing of the binary phase plates.

APPENDIX A

The photographs in Figs. 9(a) and 9(b) show the binary phaseplates, the halves and the quadrants, respectively, The photographs provide an experimental confirmation of the $\lambda/2$ phase lag. They are recorded at the output of an interferometer (Zeiss, Oberkochen, Germany) at a wavelength of 644 nm, as provided by a Cadmium lamp. The two interfering wave fronts of illumination are tilted by a finite angle to produce interference fringes. Outside the phase retarding regions the interference fringes are straight lines, indicating that the glass substrate of the filter obeys a flatness of better than $\lambda/10$. Since the wavelength of 644 nm is close to the STED wavelength for which the retarding plates are designed, the interference fringes are shifted about a half of a period. The circular shape of the rear aperture of the objective lens and its relative size is indicated by a circle.

[1] E. Abbe, Arch. f. Mikroskop. Anat. **9**, 413 (1873).
[2] E. Abbe, *Gesammelte Abhandlungen* (G. Fischer, Jena, 1904).
[3] G. Toraldo di Francia, Nuovo Cimento, Suppl. **9**, 426 (1952).
[4] S. W. Hell and J. Wichmann, Opt. Lett. **19**, 780 (1994).
[5] S. W. Hell, in *Topics in Fluorescence Spectroscopy*, edited by J. R. Lakowicz (Plenum, New York, 1997), Vol. 5, p. 361.
[6] T. A. Klar and S. W. Hell, Opt. Lett. **24**, 954 (1999).
[7] T. A. Klar, S. Jakobs, M. Dyba, A. Egner, and S. W. Hell, Proc. Natl. Acad. Sci. U.S.A. **97**, 8206 (2000).
[8] T. A. Klar, M. Dyba, and S. W. Hell, Appl. Phys. Lett. **78**, 393 (2001).
[9] J. R. Lakowicz, I. Gryczynski, J. Kusba, and V. Bogdanov, Photochem. Photobiol. **6**, 546 (1994).
[10] M. Born and E. Wolf, *Principles of Optics* (Pergamon, Oxford, 1993).
[11] B. Richards and E. Wolf, Proc. R. Soc. London, Ser. A **253**, 358 (1959).
[12] M. Schrader, F. Meinecke, K. Bahlmann, M. Kroug, C. Cremer, E. Soini, and S. W. Hell, Bioimaging **3**, 147 (1995).
[13] S. C. Tidwell, H. F. Dennis, and W. D. Kimura, Appl. Opt. **29**, 2234 (1990).
[14] K. S. Youngworth and T. G. Brown, Proc. SPIE **3919**, (2000).
[15] S. W. Hell, S. Lindek, C. Cremer, and E. H. K. Stelzer, Appl. Phys. Lett. **64**, 1335 (1994).
[16] J. R. Lakowicz, *Principles of Fluorescence Spectroscopy* (Kluwer Academic, New York, 1999).
[17] M. Dyba, T. A. Klar, S. Jakobs, and S. W. Hell, Appl. Phys. Lett. **77**, 597 (2000).